Self-Propelled Robotic System with a Visco-Elastic Joint: Dynamics and Motion Analysis

Pengcheng Liu[1]*, M. Nazmul Huda[2], Zhichuan Tang[3], Li Sun[4]

*Corresponding Author: pliu@cardiffmet.ac.uk

[1] *Cardiff School of Technologies, Cardiff Metropolitan University, Cardiff CF5 2YB, United Kingdom*   *ORCID: 0000-0003-0677-4421*

[2] *School of Computing, Electronics and Mathematics, Coventry University, Coventry CV1 5FB, United Kingdom*

[3] *Industrial Design Institute, Zhejiang University of Technology, Hangzhou 310014, China*

[4] *Oxford Robotics Institute, University of Oxford, Oxford OX1 3PJ, United Kingdom*

Abstract This paper studies the dynamics and motion generation of a self-propelled robotic system with a visco-elastic joint. The system is underactuated, legless and wheelless, and has potential applications in environmental inspection and operation in restricted space which are inaccessible to human beings, such as pipeline inspection, medical assistance and disaster rescues. Locomotion of the system relies on the stick-slip effects, which interacts with the frictional force at the surface in contact. The nonlinear robotic model utilizes combined tangential-wise and normal-wise vibrations for underactuated locomotion, which features a generic significance for the studies on self-propelled systems. To identify the characteristics of the visco-elastic joint and shed light on the energy efficacy, parameter dependences on stiffness and damping coefficients are thoroughly analysed. Our studies demonstrate that dynamic behaviour of the self-propelled system is mainly periodic and desirable forward motion is achieved via identification of the variation laws of the control parameters and elaborate selection of the stiffness and damping coefficients. A motion generation strategy is developed, and an analytical two-stage motion profile is proposed based on the system response and dynamic constraint analysis, followed by a parameterization procedure to optimally generate the trajectory. The proposed method provides a novel approach in generating self-propelled locomotion, and designing and computing the visco-elastic parameters for energy efficacy. Simulation results are presented to demonstrate the effectiveness and feasibility of the proposed model and motion generation approach.

Keywords Self-propelled system, Stick-slip motions, Visco-elastic property, Motion trajectory generation, Underactuation

1. Introduction

Effective utilizations of flexible elements into the robotic locomotion have attracted significant interests in robotics and control communities. The motivations are diverse, for instance, to build up safer interactions with humans [1, 2], to improve the model accuracy of the robotic systems [3, 4], to achieve higher level of manoeuvrability, high bandwidth mechanical compliance, flexibility, agility, controllability, adaptability, and efficacy in fulfilling large scope of tasks in unstructured and hazardous environment [5–14].

Extensive endeavours have been devoted to this research domain, for instance, an optimization framework was proposed in [15] to design and analyse underactuated biped walkers, which are characterized by actuated or passive joints with rigid or non-negligible elastic actuation/transmission elements. Visco-elastic models were proposed in [16] for a soft robotic mechanism horizontally actuated by two dielectric elastomer actuators. To maximize the energy dissipated in transparent laminates under low velocity impact, a genetic algorithm was employed in [17] to optimize a model considering thermo-elasto-visco-plastic materials. In the presence of hysteresis and friction, the impact on stiffness and damping characteristics of elastic robot joints was discussed in [18]. To design an optimal motion trajectory of flexible mobile manipulators, Pontryagin's minimum principle was adopted in [19] and the optimal control issue was converted into a two point boundary value problem. There are also some significant studies on elastic robots as in [20–22]. However, for mobile systems, it is intractable that how to achieve a systematic way of utilizing the system dynamics in the forms of optimally synthesized trajectory and effectively designed controller, particularly in the presence of visco-elasticity. Structural simple systems may behave extremely rich dynamics, and even a tiny parameter variation may lead to qualitative changes of the system outputs.

Recently, there are emerging practical engineering requirements and rising research interest in nonlinear dynamics and multi-stability, as such, the vibro-impact characteristic of active mechanisms have been widely applied to a large range of engineering mechanical systems. During these applications, the correlative relationships between the system parameters and dynamic performance can be achieved. Driven by external harmonic excitations, these implementations are capable of motions such as rectilinear [23, 24] unidirectional [25] and bidirectional [24] by utilizing a periodically driven mass/inertia that interacts with the main robot body. A three-masses model was analysed and compared with a low dimensional model in [26]. More interestingly, the authors considered several system control parameters including the applied static force, the amplitude and frequency of the applied force, which were optimally chosen through the higher dimensional model simulations. As a practical application, the vibro-impact dynamics of a capsule robot was studied in [27], which consists of a capsule main body that interacts with an internally moving mass excited by harmonic force. It is revealed in [27] that the system response are mainly periodic and the best progression can be guaranteed through careful selection of the system control parameters. Notably, the dynamic models developed by these works have

been proved to be useful for uncovering the interactive dynamic performance of such systems in real-world applications. Moreover, these related works have contributed to fundamental characteristics of the non-smooth motions of practical mechanical systems with impacts. Nevertheless, it is important to note that most of these studies are, in nature, based on rectilinear motions under the consideration of visco-elastic characteristic. However, to the best of our knowledge, very few research has considered modelling, analysis and optimal parametric selection for nonlinear (rotational) motions of self-propelled system in the presence of visco-elastic characteristic.

This paper investigates the compliant property of an encapsulated self-propelled system with a visco-elastic joint. It is underactuated, legless and wheelless, and thus has potential applications in restricted space, such as pipeline inspection, medical assistance and information acquisition in disaster rescues. The proposed motion generation approach, in nature, employs a vibro-driven pendulum nonlinearly coupled with a 2-DOF spring-mass-damper system and actuated by a rotational autogenetic torque. Comparing to the self-propelled robotic systems in the literature (e.g., [25, 27, 28]), the proposed robot model employs combined tangential-wise (i.e., linearly along the direction of motion) and norm-wise vibrations for bidirectional underactuated locomotion, which features a generic significance in the studies on self-propelled robotic system. Also designing an impedance model (inertia-spring-damper) in the rotational joint of the pendulum can improve the system efficiency. Therefore, the contribution of this paper includes: (1) it conducts computation of the visco-elastic parameters under the consideration of energy-efficient locomotion; (2) it proposes the motion generation strategy of the self-propelled robotic system with detailed analysis for each motion phase; (3) it identifies the qualitative features of the system dynamics to achieve the optimal forward motion of the self-propelled robot.

This paper is organised as follows. Section 2 formulates the problem and derives the system dynamics of the self-propelled system. Section 3 investigates the dynamic behaviours of the system and identifies the variation laws of the visco-elastic elements. In Section 4, motion generation strategy and an analytical two-stage trajectory are presented with an optimization that incorporates the selected stiffness and damping coefficients, and numerical simulation results are demonstrated to verify the performance in Section 5. Finally, conclusions are outlined in Section 6.

2. The self-propelled robotic system

Consider the self-propelled system as shown in Fig. 1, where inside the shell, a vibration-driven pendulum is articulated with a linear visco-elastic pair of torsional spring and viscous damper and mounted on the top of a horizontally moving base. The mass of the pendulum is assumed centralized at the ball and the centre of mass of the base is assumed coinciding with the pivot axis. The main difference between the proposed system and the conventional cart-pole system is that the torque is applied at the pivot to rotate the pendulum with no force on the cart, which induces trajectory planning and tracking issues rather than the swinging-up or

stabilization problems. As an energy storage element, a torsional spring is employed to improve the energy efficacy through optimally designed motion trajectory of the pendulum discussed in Section 3.
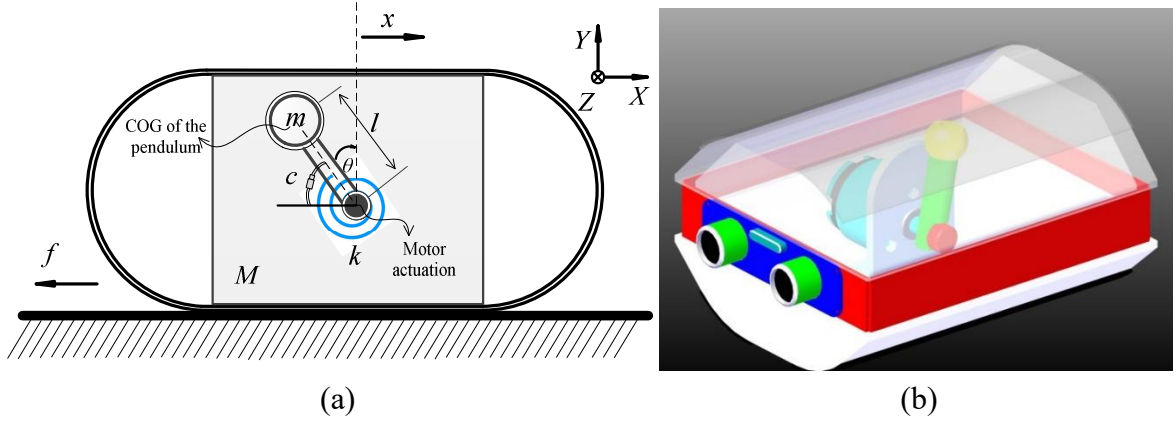

(a)   (b)

Fig.1 The self-propelled robotic model.

The robot body is driven rectilinearly over a surface by the force applied on the pendulum and the dry friction between the sliding surface, and the robot body performs sticking and slipping intermittently. The potential energy is stored and released in compatible with the compression and extension of the torsional spring. The motor torque actuation rotates the pendulum back and forth and drives the entire system moving forward through the strongly coupled force. Motion of the robot begins with a static state, and the robot moves when the magnitude of the resultant force applied on the body in the horizontal direction exceeds the maximal value of the dry friction force at the contacting surface. It is termed sticking phase when the above condition is not satisfied. The occurrence of sticking phase is diverse, at the initial static state, during the motion cycle as well as at the end. It is termed slipping phase when the magnitude of the resultant force exceeds the static resistant force, and the robot body moves forward, and the sticking phase is ended.

The torsional spring is un-stretched when the driving pendulum is at the upright position. M and m are the masses of the cart and the ball, respectively. l is the length of the inverted pendulum, θ and x depict the configuration variables of the rotational and the horizontal movements, i.e. $q = [q_1, \ q_2]^T = [\theta, \ x]^T$. k and c represent the stiffness and damping coefficients, respectively. T denotes the control input applied to the system and physically describes the motor torque that exerts on the pendulum rotation. The motor torque actuation rotates the pendulum back and forth and drives the whole system moving forward through the strongly coupled force. The forward motion of the robot emerges when the force applied in the horizontal direction exceeds the threshold of the dry friction force. The motion equations of the proposed system are derived using the Euler-Lagrangian method, and the Coulomb friction model [29] is employed to describe the resistance force between the robot and the environment surface $f_c = \begin{cases} 0, & \dot{x} = 0 \\ \mu(Mg + F_y)sgn(\dot{x}), & \dot{x} \neq 0 \end{cases}$, with μ being the friction coefficient and F_y being the internal reaction forces applied on the pendulum by the platform in the vertical direction. The friction at the pivot is assumed as a viscous friction as a function of angular velocity. It is worth mentioning that the surface in contact is anisotropic, and the asymmetry

characteristic may exist because of the physical and structural inconsistency of system parameters. As such, it is plausible that the stiction force exists with its value range falling into the threshold of the Coulomb friction $[-\mu(Mg + F_y)sgn(\dot{x}), \mu(Mg + F_y)sgn(\dot{x})]$. This is resulting from the sticking motion and largely depending on the magnitudes of the external forces.

Based on the assumptions and definitions, the governing equations of the self-propelled system are derived using Euler-Lagrangian method [30] described as

$$\frac{d}{dt}\frac{\partial L(q_i,\dot{q}_i)}{\partial \dot{q}_i} - \frac{\partial L(q_i,\dot{q}_i)}{\partial q_i} + f = Q_i \tag{1}$$

where q_i are the generalized coordinates, $L(q_i,\dot{q}_i)$ is the Lagrangian function, f describes the resistant and dissipated forces, Q_i is the generalized externally applied force or moment. Applying (1) into the proposed system and letting $q_1 = \theta$, $q_2 = x$, we have the dynamics of the system as

$$ml^2\ddot{\theta} - ml\cos\theta\ddot{x} - mgl\sin\theta + k\theta + c\dot{\theta} = T \tag{2}$$

$$-ml[\cos\theta + \mu\sin\theta sgn(\dot{x})]\ddot{\theta} + (M + m)\ddot{x} + ml[\sin\theta - \mu\cos\theta sgn(\dot{x})]\dot{\theta}^2 + \mu[(M + m)g$$
$$- (k\theta + c\dot{\theta})\sin\theta/l]sgn(\dot{x}) = 0$$

$$\tag{3}$$

Harmonic excited forces have been well-employed to generate periodic motions. By doing so, forward and backward locomotion can be obtained and controlled through appropriate design of the control parameters. Therefore, in this paper, the input torque applied on the pendulum at the pivot generates a harmonic force which is a time-varying function given by

$$T = Acos(\Omega t) \tag{4}$$

where A and Ω are amplitude and frequency of the harmonic force, respectively.

To obtain clearer numerical simulations and simplify the analysis, we introduce a dimensionless time τ, and define a series of non-dimensional parameters and scale transformations to reduce the complexity of system dynamics as follows $\tau = \omega_n t$, $X = x/l$, $\omega_n = \sqrt{g/l}$, $\omega = \Omega/\omega_n$, $\lambda = M/m$, $\rho = k/(ml^2\omega_n^2)$, $v = c/(ml^2\omega_n)$ and $h = A/(ml^2\omega_n^2)$, where ω_n is the natural frequency of the pendulum.

Adopting these parameters into Eqs. (2) and (3), and utilizing the chain rule $\frac{d\theta}{dt} = \frac{d\theta}{d\tau} \times \frac{d\tau}{dt}$ leads to the following scaled governing equations for the proposed system, which represent the motion of the inverted pendulum and the base respectively

$$\ddot{\theta} - \cos\theta\ddot{X} - \sin\theta + \rho\theta + v\dot{\theta} = h\cos(\omega\tau) \tag{5}$$

$$-[\cos\theta + \mu\sin\theta sgn(\dot{X})]\ddot{\theta} + (\lambda + 1)\ddot{X} + [\sin\theta - \mu\cos\theta sgn(\dot{X})]\dot{\theta}^2 + \mu[(\lambda + 1)$$
$$- (\rho\theta + v\dot{\theta})\sin\theta]sgn(\dot{X}) = 0$$

$$\tag{6}$$

From Eqs. (5) and (6), and letting $y_1(\tau) = \theta(\tau), y_2(\tau) = \dot{\theta}(\tau), y_3(\tau) = X(\tau), y_4(\tau) = \dot{X}(\tau)$, we have the state-space representations

$$\begin{bmatrix} \dot{y}_1(\tau) \\ \dot{y}_2(\tau) \\ \dot{y}_3(\tau) \\ \dot{y}_4(\tau) \end{bmatrix} = \begin{bmatrix} 0 & 1 & 0 & 0 \\ A_{21}/\Delta & A_{22}/\Delta & A_{23}/\Delta & A_{24}/\Delta \\ 0 & 0 & 0 & 1 \\ A_{41}/\Delta & A_{42}/\Delta & A_{43}/\Delta & A_{44}/\Delta \end{bmatrix} \begin{bmatrix} y_1(\tau) \\ y_2(\tau) \\ y_3(\tau) \\ y_4(\tau) \end{bmatrix} + \begin{bmatrix} 0 \\ B_2/\Delta \\ 0 \\ B_4/\Delta \end{bmatrix} \tag{7}$$

where

$A_{21} = -\rho(\lambda + 1) + \mu\rho siny_1 sgn(y_4)cosy_1,$

$A_{22} = -\upsilon(\lambda + 1) + [\mu cosy_1 sgn(y_4) - siny_1]y_2 cosy_1 + \mu\upsilon siny_1 sgn(y_4)cosy_1,$

$A_{23} = 0, \ A_{24} = 0,$

$A_{41} = -\rho[cosy_1 + \mu siny_1 sgn(y_4)] + \mu\rho siny_1 sgn(y_4),$

$A_{42} = [\mu cosy_1 sgn(y_4) - siny_1]y_2 - \upsilon siny_1 sgn(y_4) - \upsilon[cosy_1 + \mu siny_1 sgn(y_4)],$

$A_{43} = 0, \ A_{44} = 0,$

$B_2 = -\mu(\lambda + 1)sgn(y_4)cosy_1 + (\lambda + 1)siny_1 + (\lambda + 1)hcos(\omega\tau),$

$B_4 = -\mu(\lambda + 1)sgn(y_4) + [cosy_1 + \mu siny_1 sgn(y_4)]siny_1 + [cosy_1 + \mu siny_1 sgn(y_4)]hcos(\omega\tau),$

$\Delta = (\lambda + 1) - cosy_1[cosy_1 + \mu siny_1 sgn(y_4)].$

3. Parametric dependence analysis

In dynamical systems, bifurcation plays an important role in creations and vanishing of the equilibriums and periodic solutions. It employs a visual interpretation of how the dynamic behaviours are affected by the system parameters and how the stability of solutions changes accompanied by the varying parameters. The solutions in this section are numerically calculated to identify the most suitable qualitative motion for the forward locomotion of the self-propelled robot.
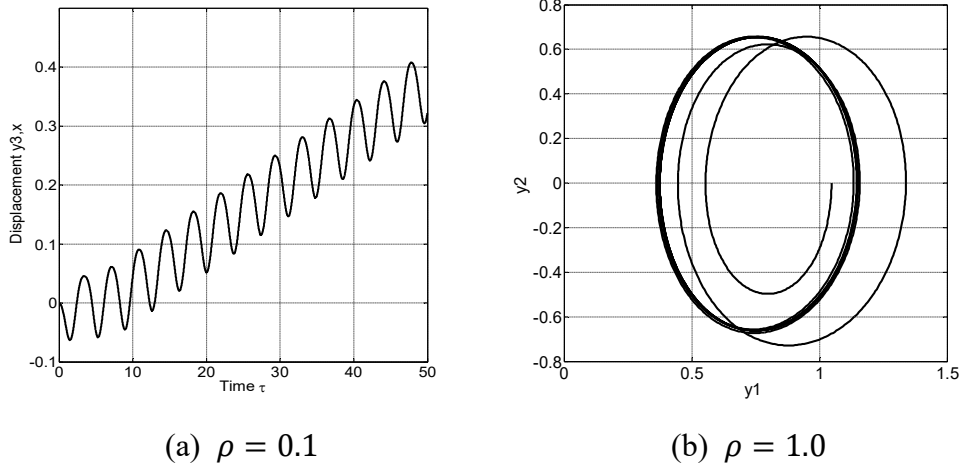

(a) $\rho = 0.1$ (b) $\rho = 1.0$

Fig. 2 Trajectories on phase plane of the self-propelled robot for $y_1(0) = \pi/3$, $h = 1.0$, $\lambda = 3.6$, $\upsilon = 0.8$ and $\omega = 1.7$.

Typical time history of the robot displacement and phase portrait of the pendulum are presented in Fig. 2(a) and Fig. 2(b), respectively. In terms of the behavioural dependence of solutions on the system parameters, the trajectories can be monitored when parameters are changing. Bifurcation analysis is then conducted to inspect traces of the solutions against the control parameters ρ and υ, respectively. First, for each value of ρ and υ, we calculate y_1 as a function of dimensionless time τ. To achieve steady state responses, the first 100 driving periods are omitted so that the initial transients have decayed away, then y_1 is plotted respectively as a function of ρ and υ. For a set of parameter values which are slightly

increased, the bifurcation scenario is studied subject to the aforementioned two parameters. Second, the first return Poincare map is created and projected respectively on the reliable axis, considering the boundedness of the state variables. The procedure is then repeated over a reasonably large range of values of ρ and υ in small steps as shown in Fig. 3 and Fig. 8, respectively.

3.1 Parameter dependence on stiffness ρ

In our previous study [24], we evident that the elastic stiffness and damping can affect the system performance, which are important factors for energy efficacy. Therefore, in this section, we aim to identify how the system behaviour is affected by these parameters, such that the optimal viscoelastic parameters are selected beforehand and fed into the parameterisation procedure of the motion trajectory. The torsional spring plays an important role in energy efficacy of the system, its stiffness coefficient is studied as a branching parameter which contributes to the elasticity on the system responses. Bifurcation diagrams are presented in Fig. 3, which depict the parameter dependence of the angular displacement (in Fig. 3(a)) and travelling velocity of the robot (in Fig. 3(b)). The Poincare maps are constructed and projected onto the y_1 and y_4 axis, respectively. It can be seen from the figure that bifurcation occurs at the stiffness coefficient ρ=0.7915, after where a large region of period-one motion is recorded for $\rho \in [0.7915, 5.1]$. During this periodic motion, angular displacement of the pendulum decreases as the value of ρ slowly increases. Fig. 3(b) demonstrates the average travelling speed which is an important index for a mobile system. We could observe that, based on the given parameter range of ρ, the maximum and minimum speed of the system.

A sequence of trajectories on the phase plane and Poincare maps are depicted in Fig. 4. The locations of Poincare section are marked by red dot. Our numerical study shows that at the relatively small coefficient as shown in Fig. 4(b), the shape of limit cycle is similar to an ellipse, when ρ >0.7915 as shown in Fig. 4(a), after the initial transients have decayed away, the pendulum employs simple but periodic motions which would repeat subsequently.
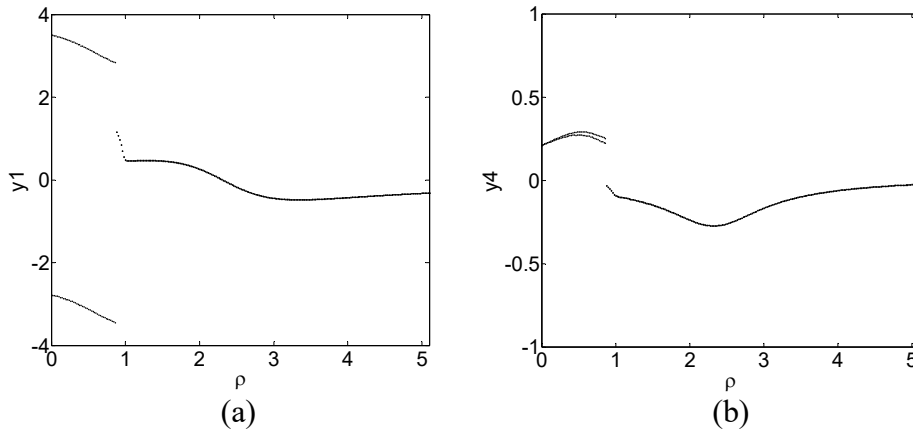

(a)   (b)

Fig. 3 Bifurcation diagrams under varying stiffness coefficient for $y_1(0) = \pi/3, h = 1.5, \lambda = 3.6, \nu = 0.8, \omega = 1.7$.

Following a similar procedure as the pendulum subsystem, the trajectories on phase plane of the robot are shown in Fig. 5, in which the average travelling velocity y_4 is plotted as a function of robot displacement y_3. The initial transient phases are also plotted here to present the traces of the self-propelled robot. It is straightforward to see that for a small stiffness coefficient, there is insufficient energy stored in the spring and injected into the self-propelled robot to enhance its forward motion, and the robot acts as atypical reciprocating motions and eventually resides within a certain boundary after initial transient has decayed away. On the other hand, for the parameters within the periodic range, as seen in Fig. 5(b), the self-propelled robot performs repeatable forward motion.

Comparison of robot travelling distance in the presence of varying stiffness coefficient is shown in Fig. 6 and Fig.7. It is observed that at relatively small values of ρ, the robot moves in periodic motion, but more like a response of vibration after the initial transients' decays (ρ =0.5, 0.7), which are equivalent to the stiffness coefficients of 0.2001 (Nm/rad) and 0.2802 (Nm/rad). When ρ crosses the critical value of gazing, the travelling distance firstly increases and then decreases monotonically accompanied by the augmented stiffness coefficient. The largest displacement of the robot is obtained for the periodic response and the optimal value is recorded at ρ =0.9, which is equivalent to the stiffness coefficient of 0.36 (Nm/rad).
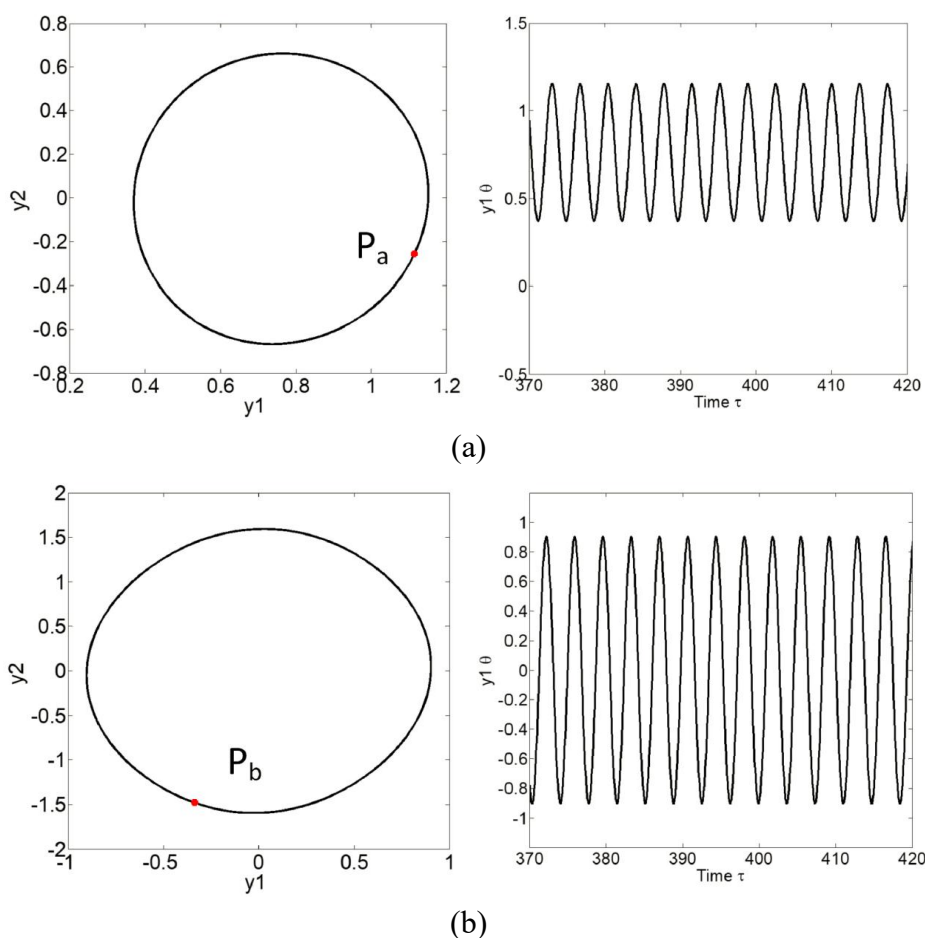

(a)

(b)

Fig. 4 Trajectories on phase plane and time histories of the pendulum for $y_1(0) = \pi/3, h = 1.0, \lambda = 3.6, v = 0.8, \omega = 1.7$.
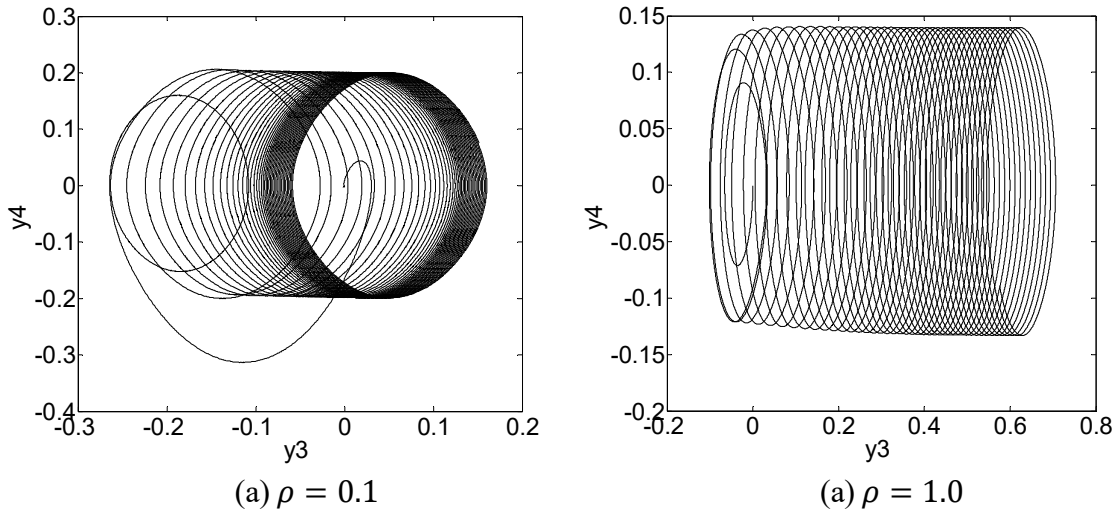
(a) $\rho = 0.1$ (a) $\rho = 1.0$

Fig. 5 The trajectories on phase plane of the capsule for $y_1(0) = \pi/3, h = 1.0,\ \lambda = 3.6, v = 0.8, \omega = 1.7$.
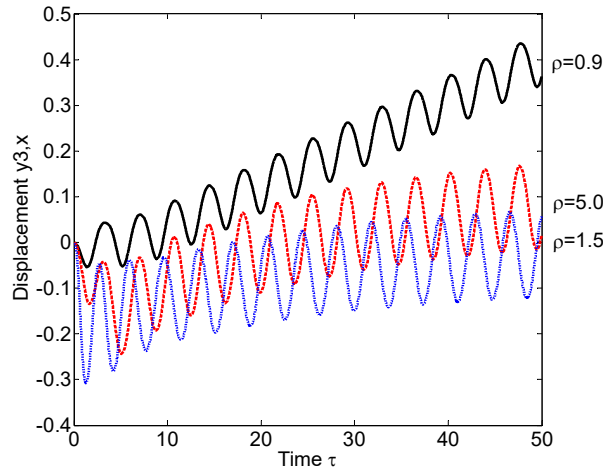

Fig. 6 Time histories of the displacements for $y_1(0) = \pi/3, h = 1.0,\ \lambda = 3.6, v = 0.8, \omega = 1.7$, obtained for varying stiffness coefficient: $\rho = 0.9,\ \rho = 1.5$ and $\rho = 5.0$.
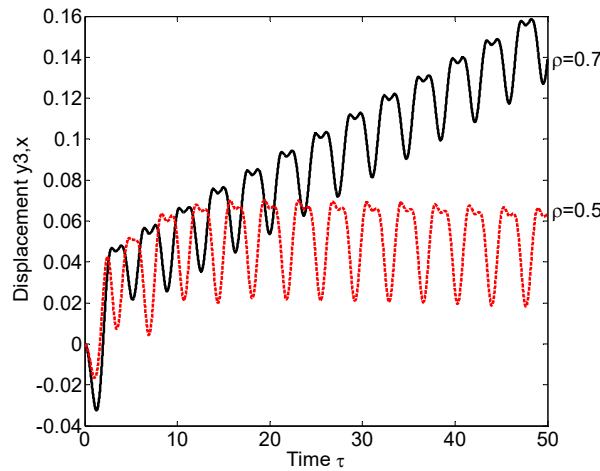

Fig. 7 Zoom up time histories of the displacements of the capsule robot for $y_1(0) = \pi/3, h = 1.0,\ \lambda = 3.6, v = 0.8, \omega = 1.7$, obtained for $\rho = 0.5$ and $\rho = 0.7$, respectively.

9

Remark 1 ρ represents the stiffness coefficient k that contributes to the energy efficacy to the self-propelled system. The boundaries of periodic system response are portrayed precisely with respect to the varying stiffness coefficient. Basically, the dependent analysis on varying stiffness shows an optimal parametric selection of the torsional spring to achieve desirable performance and avoid undesirable motions. On the other hand, difference at the periodic motions exists in the shapes and the Poincare sections of the limit cycles, which result in varying performance.

3.2 Parameter dependence on stiffness v

Parameter dependence on damping v is studied in this subsection, which describes how the viscous coefficient c affects the system performance qualitatively. The bifurcation diagrams are shown in Fig. 8. The Poincare maps are constructed and projected onto the y_2 and y_1 axis, respectively recorded the average angular velocity in Fig. 8 (a) and displacement of the pendulum in Fig. 8 (b). Herein, accompany with the increasing of the damping coefficient, the system response keeps behaving period-one motion for $v \in [0.01, 5.1]$. The variations shown in Fig. 8 indicate that the larger damping injected into the system, the less angular displacement and velocity it performs.

The trajectories of the pendulum on the phase plane and Poincare maps are shown in Fig.9. The locations of Poincare sections P_a and P_b are marked by red dots. The time histories of the angular displacement in Fig. 9 are important to appreciate the dynamic behaviours illustrated. It is noted that after the initial transients have decayed, the pendulum employs simple and repeatable periodic motion.

Furthermore, to examine the dynamic behaviour of the entire robotic system, we construct the trajectories on phase plane of the entire robot are shown in Fig. 10, in which the average forward velocity y_4 is plotted as a function of robot travelling displacement y_3. The repeatable forward motion after initial transient. It is also noted that the larger v is employed, the shorter travelling distance the robot performs.
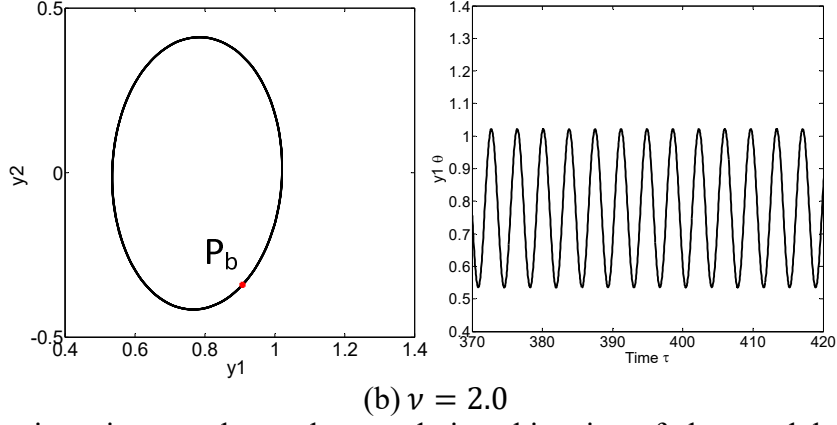

(a) $v = 0.6$

(b) $\nu = 2.0$
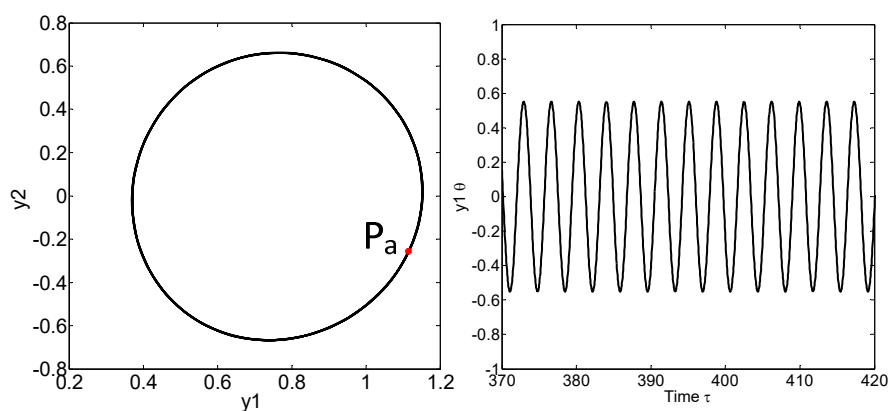
Fig. 9 The trajectories on phase plane and time histories of the pendulum for $y_1(0) = \pi/3, h = 1.0,\ \lambda = 3.6, \rho = 1.5$ and $\omega = 1.7$.
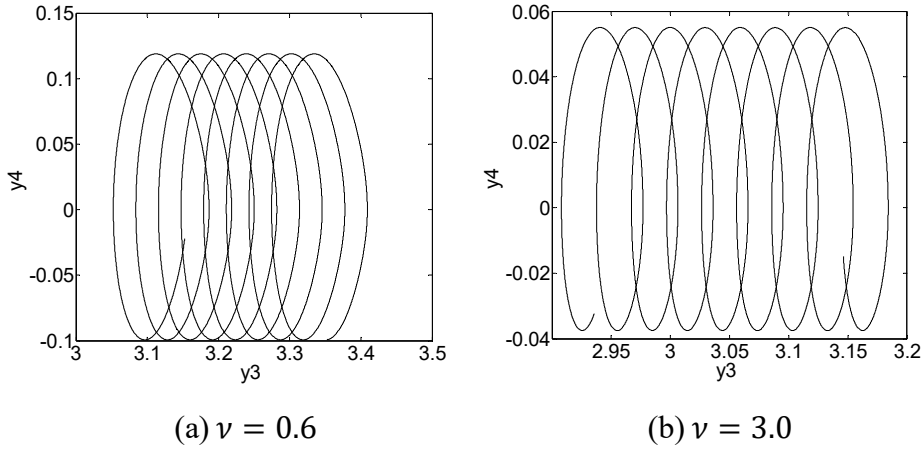

(a) $\nu = 0.6$ (b) $\nu = 3.0$

Fig. 10 The trajectories on phase plane of the capsule for $y_1(0) = \pi/3, h = 1.0,\ \lambda = 3.6, \rho = 0.9$ and $\omega = 1.7$.

The comparison of robot travelling distance in the presence of varying damping coefficient is presented in Fig. 11. It is revealed that the proposed system maintains steady-state progression after the initial transient is decayed away, and the capsule progression decreases monotonically accompanied by the augmented damping coefficient. Still, the best progression of the capsule can be obtained for the periodic response and the optimal value is recorded at ν=0.6, which is equivalent to the damping coefficient of $c = 0.0426\ (kg * m^2 * s^{-1} * rad^{-1})$.

Remark 2*:* The dependent analysis on varying damping illustrates the effect of the limiting factor on the system dynamics, which heuristically can be adopted to optimize the injection of damping to achieve desired performance and avoid undesired responses. On the other hand, the different shapes and the Poincaré sections of the limit cycles result in varying performance.
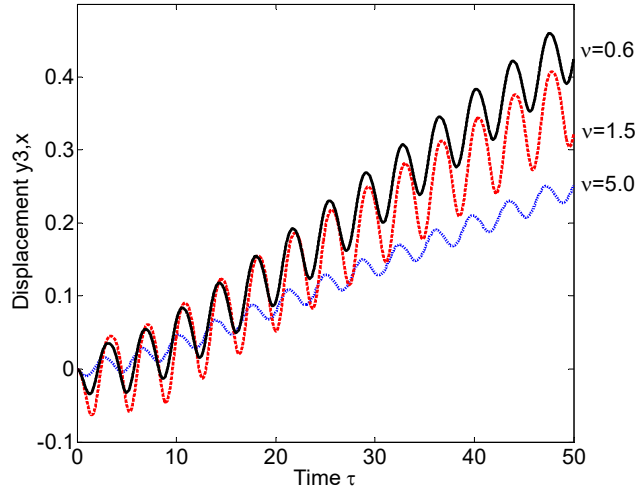
Fig. 11 Time histories of the displacements for $y_1(0) = \pi/3, h = 1, \lambda = 3.6, \rho = 0.9, \omega = 1.7$, obtained for: $\nu = 0.6, 3.5$ and $\nu = 5.0$.

4. Underactuated motion generation

4.1 The desired motion trajectory

Periodic motion are generated to synthesize the rotational motion of the pendulum and the harmonic property of the viscoelastic element. It is considered that the characteristic of viscoelastic element is equivalent to existence of the periodic trajectory manifold with homologous arguments. In particular, three stages below are designed to generate the desired periodic locomotion:

Initialization and re-initialization stages ($\tau = \tau_0, \tau_7$): one cycle of forward motion begins and ends respectively with the initialization and re-initialization stages. In the initialization stage, the pendulum and torsional spring are constrained and kept stationary at a designed angle against the opposite direction of the retraction of spring, which stores potential energy in such a manner that more mechanical power will be injected into the entire system; at the end of the motion, the pendulum gradually returns to the initial position by following the motion profile, the system then is reinitialized with stored elastic energy for the new cycle.

Forward motion stage ($\tau \in (0, \tau_3)$): the torque motor drives the pendulum fast in the forward direction, together with the energy-releasing of the torsional spring, which leads the system to overcome the maximal dry friction and therefore, a continuous movement of the robotic system is obtained;

Restoring stage ($\tau \in (\tau_4, \tau_7)$): the pendulum gradually returns to the initial angular position to restore the potential energy and prepare for the next motion cycle, the resultant force on the system as a whole in the horizontal direction is less than the maximum static friction, which means the whole system is kept stationary in this stage of duration.
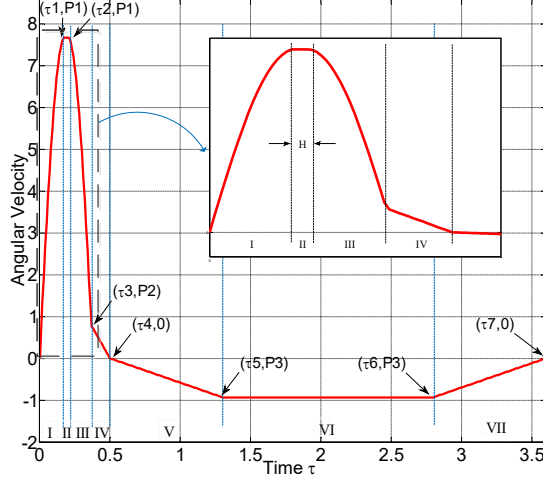
Fig. 12 Desired periodic motion trajectory for one cycle. The zoom up window demonstrates the details in the forward motion stage.

Motivated by the qualitative changes in the stability of solutions with respect to the varying parameters, it is noted that the desirable forward motions can be achieved through careful choices of the parameters, and the net travelling displacement during one full cycle is determined by the forward motion stage. Therefore, a desired periodic motion profile can be generated by Eq. (8) and shown in Fig.12.

$$
\dot{\theta}_d = \begin{cases}
P_1 \omega \sin(\omega\tau), & \tau \in [0, \tau_1) \\
P_1 \omega, & \tau \in [\tau_1, \tau_2) \\
P_1 \omega \sin(\omega\tau - \tau_2), & \tau \in [\tau_2, \tau_3) \\
\dfrac{\tau_3 - \tau}{\tau_3 - \tau_2} P_2, & \tau \in [\tau_3, \tau_4) \\
\dfrac{\tau_3 - \tau}{\tau_4 - \tau_3} P_3, & \tau \in [\tau_4, \tau_5) \\
-P_3, & \tau \in [\tau_5, \tau_6) \\
\dfrac{\tau_6 - \tau}{\tau_5 - \tau_6} P_3, & \tau \in [\tau_6, \tau_7)
\end{cases}
\tag{8}
$$

It is apparent that a parametric selection procedure is needed to obtain the time-varying reference motion trajectory (8), and accordingly a series of parameters including the time durations τ_1 - τ_7, the maximum angular velocity of the periodic trajectory in scaled coordinate P_1, its minimum counterpart P_2 as well as the critical angular velocity P_3 when the robot begins to keep stationary.

Detailed description of each phase of the motion trajectory profile is listed as follows:

Initialization $\tau = \tau_0$: $\theta(\tau) = \theta_{min} = -\theta_0$, $\dot{\theta}(\tau) = 0$, $\ddot{\theta}(\tau) = 0$, $X(\tau) = 0$, $\dot{X}(\tau) = 0$, $\ddot{X}(\tau) = 0$. The pendulum and torsional spring are kept stationary at a designed negative angle θ_0 to the opposite direction of the retraction of spring, which stores potential energy such that more mechanical power will be provided.

Phase I $\tau \in (\tau_0, \tau_1)$: $\theta(\tau) = \theta > 0$, $\dot{\theta}(\tau) > 0$, $\ddot{\theta}(\tau) \gg 0$, $X(\tau) = x$, $\dot{X}(\tau) > 0$, $\ddot{X}(\tau) > 0$. The torque motor begins to move under the synthesized angular velocity and simultaneously the stored potential energy is released from the stretched torsional spring. This results in a motion with maximal angular acceleration of the pendulum pushing the base moving forward with relatively high acceleration.

13

Phase II $\tau \in [\tau_1, \tau_2)$: $\theta(\tau) = \theta > 0$, $X(\tau) = x$, $\dot{\theta}(\tau) > 0$, $\dot{X}(\tau) > 0$, $\ddot{\theta}(\tau) = 0$, $\ddot{X}(\tau) > 0$. It is noted that once the potential energy is released, a short period of time is required to let the potential energy fully transfer into kinetic energy of the proposed system. This leads to more efficient energy consumption. Thus a short period of uniform motion of the pendulum is designed. During this period, the pendulum swings forward with the maximal angular velocity while driving the base accelerating continuously.

Phase III $\tau \in [\tau_2, \tau_3)$: $\theta(\tau) = \theta > 0$, $\dot{\theta}(\tau) > 0$, $\ddot{\theta}(\tau) < 0$, $X(\tau) = x$, $\dot{X}(\tau) > 0$, $\ddot{X}(\tau) < 0$. The torque actuation exerts an opposing force on the pendulum under the synthesized angular velocity together with the contraction of the torsional spring. This leads to a forward deceleration motion of the pendulum as well as the base.

Phase IV $\tau \in [\tau_3, \tau_4)$: $\theta(\tau) = \theta_{max} > 0$, $\dot{\theta}(\tau) \to 0$, $\ddot{\theta}(\tau) < 0$, $X(\tau) = x \to 0$, $\dot{X}(\tau) = 0$, $\ddot{X}(\tau) = 0$. In this phase, a slow deceleration motion of the pendulum results in the stationary of the base, which is subjected to the constraints under the dissipative force lie in the sliding surface as well as the pivot. Moreover, the angular displacement of the pendulum is constrained at θ_{max} to avoid over-actuation and system failure.

Phase V $\tau \in [\tau_4, \tau_5)$: $\theta(\tau) = \theta < 0$, $\dot{\theta}(\tau) < 0$, $\ddot{\theta}(\tau) < 0$, $X(\tau) = x$, $\dot{X}(\tau) = 0$, $\ddot{X}(\tau) = 0$. Phase V is designed to be a short duration and to generate a relatively low angular acceleration of the pendulum which keeps the base stands still.

Phase VI $\tau \in [\tau_5, \tau_6)$: $\theta(\tau) = \theta < 0$, $\dot{\theta}(\tau) = -P_3 < 0$, $\ddot{\theta}(\tau) = 0$, $\mathrm{X}(\tau) = a\Delta x$, $\dot{X}(\tau) = 0$, $\ddot{X}(\tau) = 0$. A uniform angular velocity of is designed for the purpose of gradually stretching the torsional spring such that enough potential energy is restored for the next cycle. The base remains stationary in this phase. $a\Delta x$ represents the net displacement of the base after the ath cycle.

Phase VII $\tau \in [\tau_6, \tau_7)$: $\theta(\tau) = \theta < 0$, $-P_3 < \dot{\theta}(\tau) < 0$, $\ddot{\theta}(\tau) > 0$, $X(\tau) = a\Delta x$, $\dot{X}(\tau) = 0$, $\ddot{X}(\tau) = 0$. In phase VII, a low angular deceleration motion is generated in a short duration to decelerate the pendulum while the base keeps stationary.

Re-Initialization $\tau = 0$: $\theta(\tau) = \theta_{min} = -\theta_0$, $\dot{\theta}(\tau) = 0$, $\ddot{\theta}(\tau) = 0$, $X(\tau) = a\Delta x$, $\dot{X}(\tau) = 0$, $\ddot{X}(\tau) = 0$. When the pendulum reaches to the initial angle, the torsional spring is constrained to θ_{min} such that enough elastic energy is stored for the next cycle.

The net forward travelling during one motion cycle is generated in the forward motion stage. Moreover, as one of the key elements regarding to the forward motion of the whole system, the friction between the platform and the sliding surface is taken into account for designing the restoring stage through the consideration of the system constraints. The proposed motion generation strategy can be utilized for generating a class of appropriate trajectory profiles for self-propelled underactuated mechanical systems with viscoelastic elements.

4.2 System constraints analysis

The optimal forward motions of the self-propelled robot in terms of travelling distance and energy consumption depend on a desirable solution for the actuated subsystem $\theta(\tau_i)$, and

also the constraints need to be integrated with the system dynamics. The robot moves in a stick-slip motion pattern on the sliding surface, thus we apply a constraint for the contacting force to guarantee that the robot's locomotion is on the horizontal surface and no vertical movement is allowed. This means the contact force has to be greater than zero and gives an inequality constraint as

$$F_y = (\lambda + 1) - sin\theta\ddot{\theta} - cos\theta\dot{\theta}^2 - \rho\theta sin\theta > 0, \ \tau \in [\tau_1, \tau_7) \tag{9}$$

In the restoring stage, the robot is kept stationary on the ground. As such, the force that the pendulum applies on the base in the horizontal direction has to be less than the maximal static friction, that is,

$$|F_x| \leq \mu|F_y|, \tau \in [\tau_5, \tau_7) \tag{10}$$

which gives a non-dimensionalized inequality constraint as

$$\left|cos\theta\ddot{\theta} - sin\theta\dot{\theta}^2 + \rho\theta cos\theta\right| \leq \mu\left|[(\lambda + 1) - sin\theta\ddot{\theta} - cos\theta\dot{\theta}^2 - \rho\theta sin\theta]\right| \tag{11}$$

Furthermore, the interactive force from vertical F_y is implicitly restricted to be non-negative under the constraint above, which essentially in virtue of the unidirectional property of the ground.

4.3 Parametric optimization

In this section, the optimal parametric selection is conducted to achieve the periodic motion trajectory. Adopting the optimal values of stiffness and damping coefficients, subsequently, a series of parameters values including $\tau_1 \sim \tau_7$, P_1, P_2 and P_3 are to be optimized. To achieve motions of the base and the pendulum, integrating (6) once in one full cycle, we have

$$(\lambda + 1)\dot{X} + \mu(\lambda + 1)sgn(\dot{X})\tau - \dot{\theta}cos\theta - \mu\dot{\theta}sin\theta sgn(\dot{X}) - \mu\rho sgn(\dot{X})\int_0^\tau \theta sin\theta d\tau$$

$$- \int_0^\tau \mu\rho h cos\omega\tau sin\theta sgn(\ddot{X})d\tau + \mu v sgn(\dot{X})\left(\theta sin\theta - \int_0^\tau \theta cos\theta d\tau\right)$$

$$- \int_0^\tau \mu v h\omega sin\omega\tau sin\theta sgn(\dot{X})d\tau - C_1 = 0$$

$$\tag{12}$$

Accordingly, the velocity of the capsule and the pendulum are given by

$$\dot{X}(\tau)$$
$$= \frac{\dot{\theta}cos\theta + \mu\dot{\theta}sin\theta sgn(\dot{X}) + \mu\rho sgn(\dot{X})\int_0^\tau \theta sin\theta d\tau + \mu v sgn(\dot{X})(\theta sin\theta - \int_0^\tau \theta cos\theta sgn(\dot{X})d\tau)}{(\lambda + 1)}$$
$$+ \frac{\int_0^\tau \mu\rho h cos\omega\tau sin\theta sgn(\dot{X})d\tau + \int_0^\tau \mu v h\omega sin\omega\tau sin\theta sgn(\dot{X})d\tau + C_1}{(\lambda + 1)} - \mu\tau sgn(\dot{X})$$

$$\tag{13}$$

$$\dot{\theta}(\tau) = \frac{(\lambda + 1)\dot{X} + \mu(\lambda + 1)sgn(\dot{X})\tau - \mu\rho sgn(\dot{X})\int_0^\tau \theta sin\theta d\tau + \mu v sgn(\dot{X})(\theta sin\theta - \int_0^\tau \theta cos\theta d\tau)}{cos\theta + \mu sin\theta sgn(\dot{X})}$$
$$- \frac{\int_0^\tau \mu\rho h cos\omega\tau sin\theta sgn(\dot{X})d\tau + \int_0^\tau \mu v h\omega sin\omega\tau sin\theta sgn(\dot{X})d\tau - C_1}{cos\theta + \mu sin\theta sgn(\dot{X})}$$

$$\tag{14}$$

Remark 3: Revisiting the desired motion trajectory shown in Fig. 12, in the progressive stage (phase *I* to phase *III*), the velocity of the capsule is greater than zero ($\dot{X}(\tau) > 0$); on the other hand, in the

15

restoring stage (phase IV to phase VII), the capsule is standstill preparing for the next progression, which means its velocity equals zero ($\dot{X}(\tau) = 0$). And the net progression during one cycle of motion is determined by the progression stage. Therefore, considering the characteristic of the sign function, the displacement of the capsule system can be obtained through integrating (8) twice, we have

$$X(\tau) = \frac{sin\theta - \mu cos\theta + \mu\rho \int_0^\tau \int_0^\tau \theta sin\theta d\tau \, d\tau + \mu v \int_0^\tau \int_0^\tau \dot{\theta} sin\theta d\tau \, d\tau + C_1(\tau) + C_2}{(\lambda + 1)}$$
$$+ \frac{\int_0^\tau \int_0^\tau \mu\rho h cos\omega\tau sin\theta d\tau \, d\tau + \int_0^\tau \int_0^\tau \mu v h\omega sin\omega\tau sin\theta d\tau \, d\tau}{(\lambda + 1)} - \frac{1}{2}\mu\tau^2, \tau \in (\tau_1, \tau_7)$$

$$(15)$$

Considering the constraints analysis, the boundary conditions are defined below

$$\theta(\tau)_{|\tau=\tau_0} = \theta(\tau)_{|\tau=\tau_7} = -\theta_0 < 0, \theta(\tau)_{|\tau=\tau_3} = \theta_0, \dot{\theta}(\tau)_{|\tau=\tau_0} = 0, \dot{X}(\tau)_{|\tau=\tau_0} = \dot{X}(\tau)_{|\tau=\tau_3}$$
$$= \dot{X}(\tau)_{|\tau=\tau_7} = 0$$

To avoid from periodic to chaotic behaviours, the desired maximal angular velocity P_1 and frequency of harmonic excitation ω can be determined based on the aforementioned nonlinear dynamic analysis. Recalling the desired periodic motion profile, in the duration$[0, \tau_3]$, P_2 can be obtained using Eq. (14) under the consideration of θ_0 that if $cos\theta + \mu sin\theta \neq 0$, yields

$$P_2 = \dot{\theta}(\tau)_{|\tau=\tau_3} = \frac{\mu(\lambda + 1)\tau_3 - \mu\rho \int_0^{\tau_3} \theta sin\theta d\tau + \mu v(\theta sin\theta - \int_0^{\tau_3} \theta cos\theta d\tau)}{cos\theta_0 + \mu sin\theta_0}$$

$$(16)$$

Furthermore, we can obtain the following relationships utilizing the conservation of the energy described in Fig. 12, yields

$$\int_0^{\tau_1} P_1\omega sin(\omega\tau)d\tau + P_1\omega(\tau_2 - \tau_1) + \int_{\tau_2}^{\tau_3} P_1\omega sin(\omega\tau - \tau_2)d\tau - \frac{1}{2}P_2[\frac{N\pi}{\omega} + \tau_2 - \tau_3] = 2\theta_0$$

$$(17)$$

$$-P_3(\tau_7 - \tau_4 + \tau_6 - \tau_5) = P_2(\tau_4 - \tau_3) + 4\theta_0 \qquad (18)$$

Proceeding one step further leads to

$$P_2 = \frac{2P_1[1 - cos(\omega\tau_1) + \omega(\tau_2 - \tau_1) + cos(\omega\tau_2) - cos(\omega\tau_3 - \tau_2)] - 4\theta_0}{\frac{N\pi}{\omega} + \tau_2 - \tau_3} \qquad (19)$$

$$P_3 = \frac{4\theta_0 + P_2(\tau_4 - \tau_3)}{(\tau_7 - \tau_4) + (\tau_6 - \tau_5)} \qquad (20)$$

For phase I, recalling the constraint of non-bounding motion, gives

$$\theta(\tau)_{|\tau=\tau_1}\left(\ddot{\theta}(\tau)_{|\tau=\tau_1} + \sqrt{\ddot{\theta}(\tau)^2_{|\tau=\tau_1} + \dot{\theta}(\tau)^4_{|\tau=\tau_1}}\right) < \varpi \qquad (25)$$

where

$$\dot{\theta}(\tau)_{|\tau=\tau_1} = P_1\omega, \ \ddot{\theta}(\tau)_{|\tau=\tau_1} = 0, \ \dddot{\theta}(\tau)_{|\tau=\tau_1} = P_1\omega\tau_1 \qquad (21)$$

Then the maximal boundary of period I can be obtained as

$$\tau_1 = \varpi/(P_1\omega)^3 \qquad (22)$$

where $\varpi = (\lambda + 1)^2/2\rho$.

In terms of phase II, we have

16

$$P_1\omega\sin(\omega\tau_3 - \tau_2) = P_2 \tag{23}$$

The duration can be calculated as

$$\tau_2 = \omega\tau_3 - arcsin(P_2/P_1\omega) \tag{24}$$

In view of the nonlinear analysis in section 3, the desired periodic motion of the pendulum in progressive stage, i.e. $\tau \in (0, \tau_3)$, is designed to reach the amplitude of the harmonic excitation torque at time τ_1 and keep it till the time τ_2, and the duration of this phase is synthesized to be half of the motion period of the excitation, which gives the duration phase III as

$$\tau_3 = N\pi/\omega \tag{25}$$

Revisiting Eq. (15), it is intuitively clear that the maximal net progression of the capsule can be achieved through enlarging the angular displacement of the pendulum as well as shortening the duration of progressive stage.

For phase IV, the capsule is kept stationary which allows a recovery process without backward motion, thus considering the constraint of non-sliding motion at time τ_3 that

$$\theta(\tau)_{|\tau=\tau_3}[\ddot{\theta}(\tau)_{|\tau=\tau_3} + \dot{\theta}(\tau)^2_{|\tau=\tau_3}] \leq \varpi\vartheta \tag{26}$$

where $\theta(\tau)_{|\tau=\tau_3} = P_2\tau_3, \dot{\theta}(\tau)_{|\tau=\tau_3} = P_2, \ddot{\theta}(\tau)_{|\tau=\tau_3} = -P_2/(\tau_4 - \tau_3)$

Therefore,

$$\tau_4 = \frac{1}{P_2 - \frac{\varpi\vartheta}{P_2{}^2\tau_3}} + \tau_3 \tag{27}$$

In terms of phase V, revisiting non-sliding motion constraint at time τ_5, yields

$$\theta(\tau)_{|\tau=\tau_5}[\ddot{\theta}(\tau)_{|\tau=\tau_5} + \dot{\theta}(\tau)^2_{|\tau=\tau_5}] \leq \varpi\vartheta \tag{28}$$

where $\ddot{\theta}(\tau)_{|\tau=\tau_5} = 0, \dot{\theta}(\tau)_{|\tau=\tau_5} = P_3, \theta(\tau)_{|\tau=\tau_5} = P_3\tau_5$

Then the maximal boundary of phase V can be obtained as

$$\tau_5 = \varpi\vartheta/P_3{}^3 \tag{29}$$

Another relationship can be achieved in the period of $[\tau_4, \tau_5]$ as

$$P_2(\tau_5 - \tau_4) = P_3(\tau_4 - \tau_3) \tag{30}$$

To parameterize the durations for phase VI and phase VII, according to the design objectives, the durations of $[\tau_4, \tau_5]$ and $[\tau_6, \tau_7]$ are accordant, which have the relationship reads

$$\tau_6 = [4\theta_0 + \tau_4(P_2 + 2P_3) - P_2\tau_3]/2P_3 \tag{31}$$

$$\tau_7 = [4\theta_0 - P_2\tau_3 + P_2\tau_4 + 2P_3\tau_5]/2P_3 \tag{32}$$

5. Simulation studies

In this section, numerical simulations are presented to verify the effectiveness of the proposed novel self-propelled robotic system when adopting the aforementioned optimized visco-elastic parameters and motion trajectory, by implementing a closed-loop tracking controller.

The optimally selected parameter values are shown in Table 1. Herein firstly, instead of a traditional displacement-velocity phase plane, the average forward velocity is plotted as a function of angular displacement and angular velocity, respectively as described in Fig. 13 (a) and Fig. 13 (b), where paint likewise the periodic motions after the initial transient is decayed away. Therefore, for a

set of optimized parameter values, the qualitative changes of the system dynamics are well recorded, and the quantitative variations of the excitation amplitudes are also precisely portrayed.

Table 1
Parameters of the numerical simulation

Parameter	Value
M	$0.5\ (kg)$
m	$0.138\ (kg)$
l	$0.3\ (m)$
g	$9.81\ (m * s^{-2})$
μ	$0.01\ (N * m^{-1}s^{-1})$
ρ	0.9
υ	0.6
h	1.0
ω	1.7
λ	3.6
ω_n	$5.7184\ (rad * s^{-1})$
t_1	$0.133\ (s)$
t_2	$0.195\ (s)$
t_3	$0.275\ (s)$
t_4	$0.9\ (s)$
t_5	$1.7\ (s)$
t_6	$5.8\ (s)$
t_7	$6.6\ (s)$

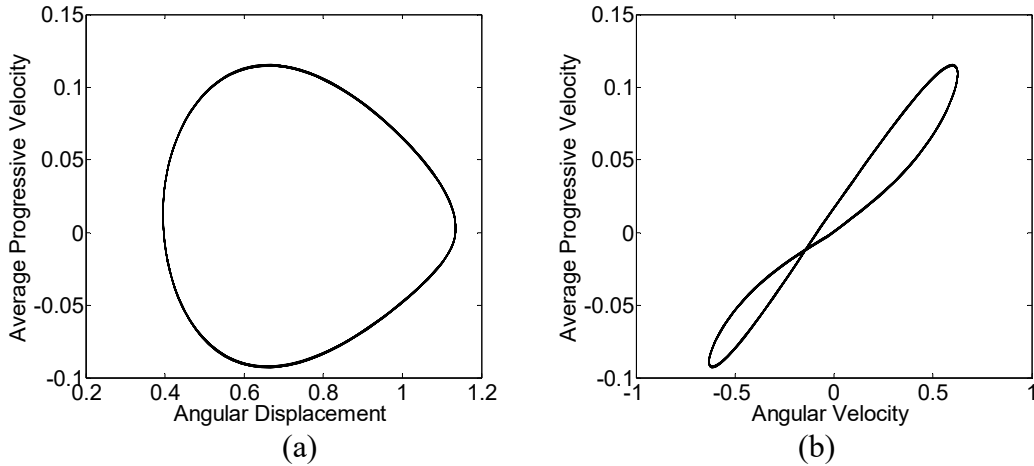(a)   (b)

Fig.13 Steady-state periodic motion trajectorie: the average progressive velocity is plotted as a function of angular displacement (a) and angular velocity (b), respectively.

On the other hand, to achieve a numerical investigation of the proposed system intuitively, a series of performance comparisons are then carried out with the system presented in [31], which is referred to as PDC system. Figs. 14 (a) and (b) depict the time histories of robot displacement and the input torque for one cycle, by tracking the desired periodic motion trajectory, the proposed system behaves steady intermittent forward motions. One can also perceive from Figs. 14 (c) and (d) that the proposed system travels 20.7588cm, while the PDC system moves 17.4865cm, with a relative displacement of 5.0957cm, which means the proposed system has a higher efficiency of 15.76% in travelling distance. In terms

of the energy consumption observed from Fig. 14 (d), the maximum input torque respectively for the proposed system and PDC system is 0.4582N*m and 0.5037N*m. The maximum angular displacement respectively for the proposed system and PDC system is 1.2059rad and 1.2775rad. On average, the optimized periodic trajectory requires only 0.5525J of the energy necessary to perform the desired trajectory, and has 16.46% higher energy efficiency than the PDC system (0.6435J).
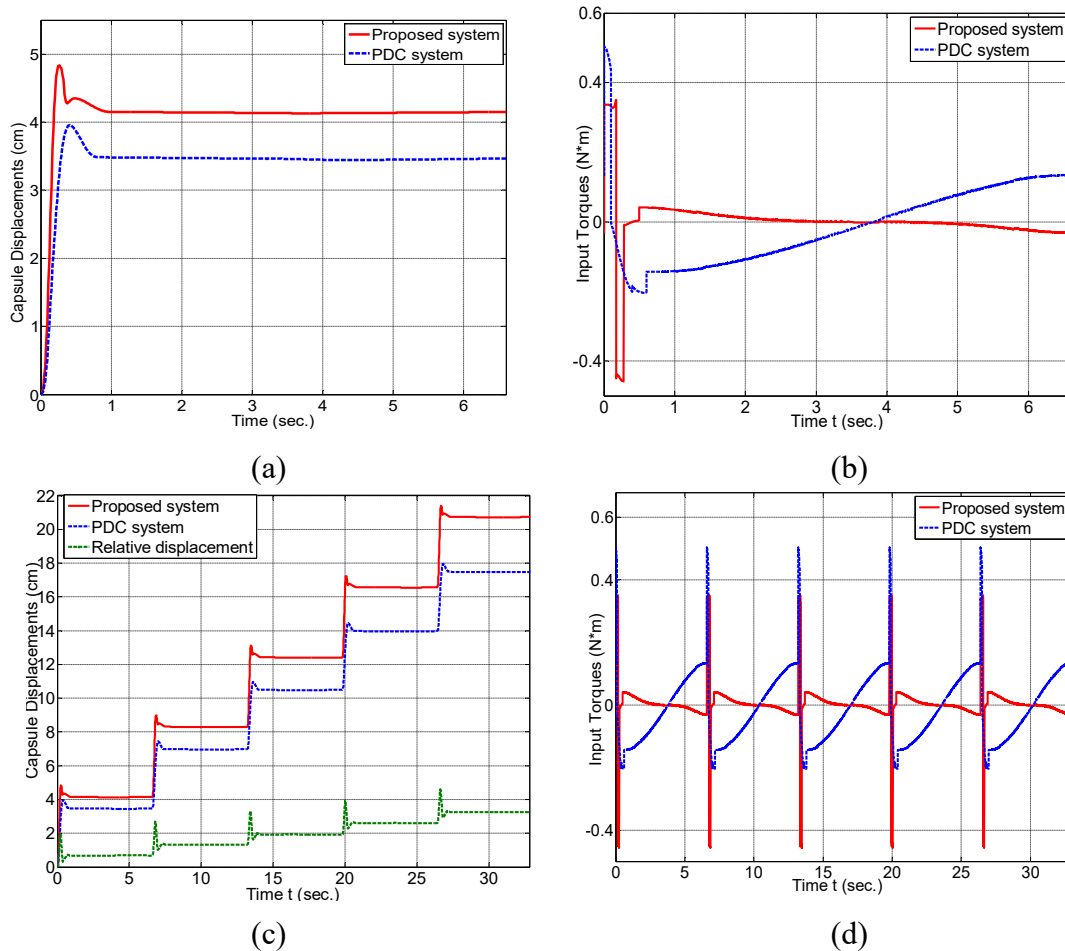

Fig. 14 Time histories of capsule displacement and input torque respectively for one cycle (a and b) and five cycles (c and d).

6. Conclusions

This paper investigates the dynamics and motion generation of a self-propelled robotic system in the presence of visco-elasticity. We show comprehensive numerical analysis of the parameter dependence on varying stiffness and damping coefficients. The bifurcation diagrams are with the most represented periodic solutions and demonstrated the thresholds of periodic motions. Our numerical studies have revealed that the behaviour of the system is mainly periodic, and the desirable travelling distance can be achieved by an appropriate selection of system parameters. The selected parameters were further adopted into the trajectory optimization to achieve promising performance with respect to the robot travelling distance and the energy consumption.

Through the investigation of varying stiffness coefficient ρ, a large region of periodic motions were found. The bifurcation is observed at $\rho = 0.7915$. The maximum average forward motion was observed at $\rho = 0.9$, where the robot experiences period-one motion. When ρ crosses the critical value of gazing, the robot displacement increases and then decreases monotonically accompanied by the augmented stiffness coefficient. The bifurcation analysis on the varying damping coefficient υ indicates that the system behaves periodic motion for all the considered set of parameter values, and the maximum average forward motion was recorded at $\upsilon = 0.6$. As the damping coefficient increases, the driving efficiency of the pendulum was reduced and subsequently, the average forward motion was decreased.

By incorporating with the selected viscoelastic parameters and system constraints analysis, an optimization procedure has been carried out to parameterize the trajectory profile. This has shed light on the relation between visco-elasticity and the optimal periodic motion trajectory, particularly for the efficient locomotion. It is noted that, using the proposed approach, the system performance is significantly improved, which is 15.76% in travelling distance and 16.46% in energy consumption. Without loss of generality, it provides a promising way that the proposed work can be extended to the study of self-propelled underactuated systems in a generic manner, which will be scrutinized in our future works. The optimization conducted in this work is based on qualitative analysis and analytical studies on the system dynamics. We will emphasize on optimization of the viscoelastic parameters, user designed parameters (e.g, critical boundaries of the trajectory and controller gains) by introducing some on-line learning algorithms and defining the objective functions.

References

1. Kong K, Bae J, Tomizuka M (2012) A compact rotary series elastic actuator for human assistive systems. *IEEEASME Trans Mechatron* 17:288–297

2. Yu H, Huang S, Chen G, et al (2015) Human–robot interaction control of rehabilitation robots with series elastic actuators. *IEEE Trans Robot* 31:1089–1100

3. Paine N, Mehling JS, Holley J, et al (2015) Actuator control for the NASA-JSC Valkyrie humanoid robot: A decoupled dynamics approach for torque control of series elastic robots. *J Field Robot* 32:378–396

4. Khosravi MA, Taghirad HD (2014) Dynamic modeling and control of parallel robots with elastic cables: singular perturbation approach. *IEEE Trans Robot* 30:694–704

5. Korayem MH, Yousefzadeh M, Beyranvand B (2017) Dynamics and control of a 6-dof cable-driven parallel robot with visco-elastic cables in presence of measurement noise. *J Intell Robot Syst* 88:73–95

6. Elgammal AT, Fanni M, Mohamed AM (2017) Design and analysis of a novel 3d decoupled manipulator based on compliant pantograph for micromanipulation. *J Intell Robot Syst* 87:43–57

7. Lam TL, Xu Y (2011) A flexible tree climbing robot: Treebot-design and implementation. In: *Robotics and Automation (ICRA), 2011 IEEE International Conference on*. IEEE, pp 5849–5854

8. Liu P, Neumann G, Fu Q, et al (2018) Energy-Efficient Design and Control of a Vibro-Driven Robot. In: *2018 IEEE/RSJ International Conference on Intelligent Robots and Systems (IROS)*. IEEE, pp 1464–1469

9. Grebenstein M, Chalon M, Friedl W, et al (2012) The hand of the DLR hand arm system: Designed for interaction. *Int J Robot Res* 31:1531–1555

10. Kolhe JP, Shaheed M, Chandar TS, Talole SE (2013) Robust control of robot manipulators based on uncertainty and disturbance estimation. *Int J Robust Nonlinear Control* 23:104–122

11. Liu P, Yu H, Cang S (2018) Optimized adaptive tracking control for an underactuated vibro-driven capsule system. *Nonlinear Dyn* 94:1803–1817

12. Liu P, Yu H, Cang S (2018) Trajectory Synthesis and Optimization of an Underactuated Microrobotic System with Dynamic Constraints and Couplings. *Int J Control Autom Syst* 1–11

13. Liu P, Yu H, Cang S (2018) On the dynamics of a vibro-driven capsule system. *Arch Appl Mech* 88:2199–2219

14. Liu P, Yu H, Cang S (2019) Modelling and analysis of dynamic frictional interactions of vibro-driven capsule systems with viscoelastic property. *Eur J Mech-ASolids* 74:16–25

15. Buondonno G, Carpentier J, Saurel G, et al (2017) Actuator design of compliant walkers via optimal control. In: *IEEE/RSJ International Conference on Intelligent Robots and Systems (IROS 2017)*. p 7p

16. Nguyen CH, Alici G, Mutlu R (2014) Modeling a soft robotic mechanism articulated with dielectric elastomer actuators. In: *Advanced Intelligent Mechatronics (AIM), 2014 IEEE/ASME International Conference on*. IEEE, pp 599–604

17. Antoine GO, Batra RC Optimization of Transparent Laminates for Specific Energy Dissipation under Low Velocity Impact using Genetic Algorithm. *Compos Struct*. https://doi.org/10.1016/j.compstruct.2014.12.066

18. Ruderman M Modeling of Elastic Robot Joints with Nonlinear Damping and Hysteresis. *Robot Syst Control Program* 293–312

19. Korayem MH, Rahimi HN, Nikoobin A (2012) Mathematical modeling and trajectory planning of mobile manipulators with flexible links and joints. *Appl Math Model* 36:3229–3244

20. Korayem MH, Ghariblu H, Basu A (2005) Dynamic load-carrying capacity of mobile-base flexible joint manipulators. *Int J Adv Manuf Technol* 25:62–70

21. Korayem MH, Nekoo SR (2015) Finite-time state-dependent Riccati equation for time-varying nonaffine systems: Rigid and flexible joint manipulator control. *ISA Trans* 54:125–144

22. Korayem MH, Shafei AM (2013) Application of recursive Gibbs–Appell formulation in deriving the equations of motion of N-viscoelastic robotic manipulators in 3D space using Timoshenko beam theory. *Acta Astronaut* 83:273–294

23. Liu P, Yu H, Cang S (2016) Modelling and dynamic analysis of underactuated capsule systems with friction-induced hysteresis. In: *Intelligent Robots and Systems (IROS), 2016 IEEE/RSJ International Conference on*. IEEE, pp 549–554

24. Liu P, Yu H, Cang S (2018) Geometric analysis-based trajectory planning and control for underactuated capsule systems with viscoelastic property. *Trans Inst Meas Control* 40:2416–2427

25. Huda MN, Yu H (2015) Trajectory tracking control of an underactuated capsubot. *Auton Robots* 39:183–198.

26. Pavlovskaia E, Hendry DC, Wiercigroch M (2015) Modelling of high frequency vibro-impact drilling. *Int J Mech Sci* 91:110–119.

27. Liu Y, Wiercigroch M, Pavlovskaia E, Yu H (2013) Modelling of a vibro-impact capsule system. *Int J Mech Sci* 66:2–11.

28. Huda MN, Yu H, Cang S (2014) Behaviour-based control approach for the trajectory tracking of an underactuated planar capsule robot. *IET Control Theory Appl* 9:163–175

29. Olsson H, Åström KJ, Canudas de Wit C, et al (1998) Friction Models and Friction Compensation. *Eur J Control* 4:176–195. https://doi.org/10.1016/S0947-3580(98)70113-X

30. Olfati-Saber R (2000) Nonlinear control of underactuated mechanical systems with application to robotics and aerospace vehicles. *Massachusetts Institute of Technology*

31. Yu H, Liu Y, Yang T (2008) Closed-loop tracking control of a pendulum-driven cart-pole underactuated system. *Proc Inst Mech Eng Part J Syst Control Eng* 222:109–125